Double-diffusive Marangoni convection in a rectangular cavity: Onset of convection

Zhi-Wu Chen,[1] Yok-sheung Li,[2] and Jie-Min Zhan[1,3,a)]
[1]*Department of Applied Mechanics and Engineering, Sun Yat-sen University, Guangzhou 510275, China*
[2]*Department of Civil and Structural Engineering, The Hong Kong Polytechnic University, Hong Kong, China*
[3]*Guangdong Province Key Laboratory of Coastal and Ocean Engineering, Guangzhou 510275, China*

(Received 20 October 2009; accepted 2 February 2010; published online 29 March 2010)

Double-diffusive Marangoni convection in a rectangular cavity with horizontal temperature and concentration gradients is considered. Attention is restricted to the case where the opposing thermal and solutal Marangoni effects are of equal magnitude (solutal to thermal Marangoni number ratio $R_\sigma=-1$). In this case a no-flow equilibrium solution exists and can remain stable up to a critical thermal Marangoni number. Linear stability analysis and direct numerical simulation show that this critical value corresponds to a supercritical Hopf bifurcation point, which leads the quiescent fluid directly into the oscillatory flow regime. Influences of the Lewis number Le, Prandtl number Pr, and the cavity aspect ratio A (height/length) on the onset of instability are systematically investigated and different modes of oscillation are obtained. The first mode is first destabilized and then stabilized. Sometimes it never gets onset. A physical illustration is provided to demonstrate the instability mechanism and to explain why the oscillatory flow after the onset of instability corresponds to countersense rotating vortices traveling from right to left in the present configuration, as obtained by direct numerical simulation. Finally the simultaneous existence of both steady and oscillatory flow regimes is shown. While the oscillatory flow arises from small disturbances, the steady flow, which has been described in the literature, is induced by finite amplitude disturbances. © *2010 American Institute of Physics*. [doi:10.1063/1.3333436]

I. INTRODUCTION

The density of a fluid can be influenced simultaneously by heat and solute with different diffusivities. In a gravitational field, this can generate many intriguing flow phenomena, even when the overall density distribution is stable. Due to its great importance in geology and many industrial processes, this double-diffusive buoyancy convection has been the topic of intensive research for many years.[1–3] Depending on the applications, different configurations of the temperature and solute concentration gradients have been considered. Only one special case is mentioned here when these gradients are both horizontal and the resultant thermal and solutal buoyancy forces are opposing and of equal magnitude (buoyancy ratio $R_\rho=-1$). In this case, a quiescent equilibrium corresponding to the pure conductive and diffusive state exists and can remain stable up to a critical thermal Rayleigh number. Krishnan[4] was the first to numerically study in a square cavity the transition from the equilibrium regime to the steady convective and time-dependent regimes. Gobin and Bennacer[5] studied the onset of convection both in an infinite vertical layer with impermeable and slip boundary conditions and in a finite cavity. A turning point of the subcritical branch was incorrectly identified as the critical bifurcation point of the quiescent equilibrium. Later Ghorayeb and Mojtabi[6] studied this problem more systematically and corrected this mistake. They numerically showed that the primary instability of the equilibrium corresponds to a transcritical bifurcation point. The onset of oscillatory flow[7] and nonlinear bifurcation analysis[8,9] have been done and extensions of the configuration to an inclined cavity[10] and to a tilted porous cavity[11] have also been considered.

In crystal growth and many other industrial processes, a liquid surface in contact with air is often present and Marangoni effects need to be taken into account. Like buoyancy force, liquid surface tension force can also be simultaneously influenced by temperature and solute concentration. While pure thermal Marangoni flow has been extensively studied,[12] much less effort has been devoted to the so-called double-diffusive Marangoni flow. The linear stability analysis of Pearson[13] was generalized by McTaggart[14] to consider simultaneously thermal and solutal Marangoni effects. It was found that when these two effects are opposing, there are circumstances under which the onset of instability is oscillatory. This analysis was extended by Ho and Chang[15] using nonlinear analysis. The linear stability characteristics of a double-diffusive fluid layer influenced by Marangoni effects were investigated by Chen and Su,[16] and the interaction between Marangoni and double-diffusive instabilities was experimentally studied by Tanny *et al.*[17] All these studies were dedicated to the situation when the temperature and concentration gradients are in the vertical direction. A stably stratified fluid layer (vertical concentration gradient) heated horizontally (horizontal temperature gradient) was studied by Chen and Chen,[18] where it was shown experimentally that salt fingers can be generated by flows driven by Marangoni

a)Author to whom correspondence should be addressed. Electronic mail: cejmzhan@gmail.com.

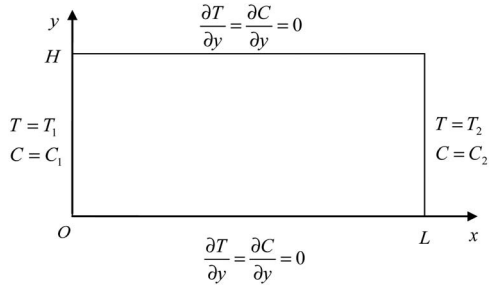

FIG. 1. Schematic of the physical system.

effects. The onset of finger convection in a similar configuration was also studied both experimentally and numerically by Chan and Chen,[19] where interaction between the thermal and solutal Marangoni effects was clearly shown.

Double-diffusive Marangoni convection in a rectangular cavity with horizontal temperature and concentration gradients was first simulated by Bergman.[20] The most important result of this study is that, in the absence of buoyancy, convection may occur, even though the overall surface tension difference along the free surface suggests stagnant fluid conditions (solutal to thermal Marangoni number ratio $R_\sigma=-1$). This situation is very similar to the above-mentioned special case in double-diffusive buoyancy convection when $R_\rho=-1$, except that the driving mechanism here is surface tension, rather than buoyancy. The quiescent equilibrium can remain stable up to a certain critical thermal Marangoni number, beyond which convection occurs. Bergman[20] obtained steady flow solution at a moderate thermal Marangoni number. Some numerical[21] and experimental[22] works have also been done for opposing thermal and solutal Marangoni effects with application to crystal growth. However, while the primary bifurcation from the equilibrium in the special case $R_\rho=-1$ has been elucidated by the work of Ghorayeb and Mojtabi,[6] the primary instability for the double-diffusive Marangoni problem with $R_\sigma=-1$ has not yet been investigated.

It is the purpose of the present paper to investigate the onset of double-diffusive Marangoni convection in a rectangular cavity with horizontal temperature and concentration gradients with $R_\sigma=-1$. It is shown by linear stability analysis that for the wide parameter range considered in the present paper, the primary instability is always a Hopf one. Thus the convection after the onset of instability is oscillatory, rather than steady. Careful direct numerical simulations are performed to validate the linear stability results and a simple physical illustration is provided to demonstrate the instability mechanism. Finally in addition to the oscillatory flow regime, it is shown that, due to finite amplitude disturbances, there coexists a steady flow regime that was first obtained by Bergman.[20]

II. PROBLEM DEFINITION

The two-dimensional rectangular cavity is made up of three rigid walls, of length L and height H and filled with a binary fluid, with a nondeformable liquid-air surface on the top (Fig. 1). Different temperatures and concentrations are specified at the left (T_1,C_1) and right (T_2,C_2) vertical walls, where $T_1>T_2$ and $C_1>C_2$, and zero heat and mass fluxes are imposed on the two horizontal boundaries. The no-slip boundary condition is adopted for all velocity components on the rigid walls, and on the upper surface the Marangoni boundary condition is applied. Boussinesq approximation is assumed to be valid except for the surface tension σ, which is allowed to vary linearly with the liquid temperature and solute concentration. Thus

$$\sigma(T,C)=\sigma_0-\gamma_T(T-T_0)-\gamma_C(C-C_0), \tag{1}$$

where $\sigma_0=\sigma(T_0,C_0)$, $\gamma_T=-(\partial\sigma/\partial T)_C$, and $\gamma_C=-(\partial\sigma/\partial C)_T$. Thermophysical properties of the fluid are estimated at the reference temperature T_0 and concentration C_0, which are set to be equal to T_2 and C_2, respectively. For the majority of mixtures, liquid surface tension increases with concentration of an inorganic solute and decreases for an organic solute. Since we are discussing double-diffusive convection in a broad sense and T and C are referred to components with higher and lower diffusivities, respectively, γ_T and γ_C can assume both positive and negative values. Buoyancy effects are neglected in the present study.

By choosing L as the unit of length and υ/L as the unit of velocity, where υ denotes kinematic viscosity of the fluid, the nondimensionalized equations governing the conservation of mass, momentums, energy, and solute concentration can be written as

$$\frac{\partial u}{\partial x}+\frac{\partial v}{\partial y}=0, \tag{2}$$

$$\frac{\partial u}{\partial t}+u\frac{\partial u}{\partial x}+v\frac{\partial u}{\partial y}=-\frac{\partial p}{\partial x}+\left(\frac{\partial^2 u}{\partial x^2}+\frac{\partial^2 u}{\partial y^2}\right), \tag{3}$$

$$\frac{\partial v}{\partial t}+u\frac{\partial v}{\partial x}+v\frac{\partial v}{\partial y}=-\frac{\partial p}{\partial y}+\left(\frac{\partial^2 v}{\partial x^2}+\frac{\partial^2 v}{\partial y^2}\right), \tag{4}$$

$$\frac{\partial \theta}{\partial t}+u\frac{\partial \theta}{\partial x}+v\frac{\partial \theta}{\partial y}=\frac{1}{\mathrm{Pr}}\left(\frac{\partial^2 \theta}{\partial x^2}+\frac{\partial^2 \theta}{\partial y^2}\right), \tag{5}$$

$$\frac{\partial c}{\partial t}+u\frac{\partial c}{\partial x}+v\frac{\partial c}{\partial y}=\frac{1}{\mathrm{Pr}\cdot\mathrm{Le}}\left(\frac{\partial^2 c}{\partial x^2}+\frac{\partial^2 c}{\partial y^2}\right), \tag{6}$$

together with boundary conditions

$$x=0,\ \ y\in[0,A]:u=v=0,\ \ \theta=c=1, \tag{7}$$

$$x=1,\ \ y\in[0,A]:u=v=0,\ \ \theta=c=0, \tag{8}$$

$$y=0,\ \ x\in[0,1]:u=v=0,\ \ \frac{\partial\theta}{\partial y}=\frac{\partial c}{\partial y}=0, \tag{9}$$

$$y=A,\ \ x\in[0,1]:v=0,\ \ \frac{\partial\theta}{\partial y}=\frac{\partial c}{\partial y}=0, \tag{10}$$

$$\frac{\partial u}{\partial y}=-\mathrm{Re}\frac{\partial\theta}{\partial x}-\mathrm{Re}_S\frac{\partial c}{\partial x}. \tag{11}$$

There are five dimensionless parameters in the above system,

$$A = \frac{H}{L},\ \mathrm{Pr} = \frac{\upsilon}{\alpha},\ \mathrm{Le} = \frac{\alpha}{D},\ \mathrm{Re} = \frac{\gamma_T \Delta T L}{\mu \upsilon},\ \mathrm{Re}_S = \frac{\gamma_C \Delta C L}{\mu \upsilon}, \tag{12}$$

which are, respectively, the aspect ratio, the Prandtl number, the Lewis number, and the thermal and solutal Reynolds numbers due to Marangoni effects. α denotes thermal diffusivity and D the molecular diffusivity. Equation (11) is the so-called Marangoni boundary condition, which equates the change in surface tension due to temperature and concentration variations across the surface to the shear stress experienced by the fluid at the surface.[13] Re and Re_S are related to the classic thermal and solutal Marangoni numbers by $\mathrm{Ma} = \mathrm{Re} \cdot \mathrm{Pr}$ and $\mathrm{Ma}_S = \mathrm{Re}_S \cdot \mathrm{Pr}$. In analogy with the buoyancy ratio R_ρ in double-diffusive buoyancy convection, the surface tension ratio in double-diffusive Marangoni convection is defined as

$$R_\sigma = \frac{\mathrm{Ma}_S}{\mathrm{Ma}} = \frac{\gamma_C \Delta C}{\gamma_T \Delta T}. \tag{13}$$

A positive value of R_σ results in augmenting convection (cooperative Marangoni forces) and a negative value leads to opposing Marangoni forces. In the present study attention is restricted to the special case $R_\sigma = -1$, in which these two forces exactly balance each other and the no-flow equilibrium solution can remain stable up to a critical thermal Marangoni number.

III. LINEAR STABILITY ANALYSIS

The linear stability characteristics of the equilibrium solution $u_0 = \upsilon_0 = 0$, $\theta_0 = 1 - x$, and $c_0 = 1 - x$ obtained for $R_\sigma = -1$ is studied. In a standard way infinitesimal disturbances are applied to the system (2)–(11) and after linearization the following system is obtained:

$$\begin{cases} \dfrac{\partial u}{\partial x} + \dfrac{\partial \upsilon}{\partial y} = 0 \\ \dfrac{\partial u}{\partial t} = -\dfrac{\partial p}{\partial x} + \nabla^2 u \\ \dfrac{\partial \upsilon}{\partial t} = -\dfrac{\partial p}{\partial y} + \nabla^2 \upsilon \\ \dfrac{\partial \theta}{\partial t} - u = \dfrac{1}{\mathrm{Pr}} \nabla^2 \theta \\ \dfrac{\partial c}{\partial t} - u = \dfrac{1}{\mathrm{Le} \cdot \mathrm{Pr}} \nabla^2 c, \end{cases} \tag{14}$$

together with boundary conditions

$$\begin{cases} x = 0, y \in [0,A]: u = \upsilon = 0, \theta = c = 0 \\ x = 1, y \in [0,A]: u = \upsilon = 0, \theta = c = 0 \\ y = 0, x \in [0,1]: u = \upsilon = 0, \dfrac{\partial \theta}{\partial y} = \dfrac{\partial c}{\partial y} = 0 \\ y = A, x \in [0,1]: \dfrac{\partial u}{\partial y} = -\mathrm{Re}\left(\dfrac{\partial \theta}{\partial x} - \dfrac{\partial c}{\partial x} \right), \\ \qquad\qquad \upsilon = 0, \dfrac{\partial \theta}{\partial y} = \dfrac{\partial c}{\partial y} = 0. \end{cases} \tag{15}$$

The independent variables u, υ, p, θ, and c now denote small disturbances. In order to eliminate the pressure terms, the stream function $\psi (\partial \psi / \partial y = u,\ -\partial \psi / \partial x = \upsilon)$ is introduced and the system becomes

$$\begin{cases} \dfrac{\partial}{\partial t} \Delta \psi = \Delta^2 \psi \\ \dfrac{\partial \theta}{\partial t} = \dfrac{\partial \psi}{\partial y} + \dfrac{1}{\mathrm{Pr}} \Delta \theta \\ \dfrac{\partial c}{\partial t} = \dfrac{\partial \psi}{\partial y} + \dfrac{1}{\mathrm{Le} \cdot \mathrm{Pr}} \Delta c, \end{cases} \tag{16}$$

with boundary conditions

$$\begin{cases} x = 0,1, y \in [0,A]: \dfrac{\partial \psi}{\partial x} = \dfrac{\partial \psi}{\partial y} = 0, \theta = c = 0 \\ y = 0, x \in [0,1]: \dfrac{\partial \psi}{\partial x} = \dfrac{\partial \psi}{\partial y} = 0, \dfrac{\partial \theta}{\partial y} = \dfrac{\partial c}{\partial y} = 0 \\ y = A, x \in [0,1]: \dfrac{\partial \psi}{\partial x} = 0, \dfrac{\partial \theta}{\partial y} = \dfrac{\partial c}{\partial y} = 0, \\ \qquad\qquad \dfrac{\partial^2 \psi}{\partial y^2} = -\mathrm{Re}\left(\dfrac{\partial \theta}{\partial x} - \dfrac{\partial c}{\partial x} \right). \end{cases} \tag{17}$$

The eigenvalue problem defined by Eqs. (16) and (17) is solved by the Tau spectral method.[23] The time dependence of disturbances is assumed to be of exponential form with a complex growth factor λ while the spatial distributions are represented by series of Chebyshev polynomials. Thus the variables are written as

$$\psi(t,x,y) = e^{\lambda t} \sum_{n=0}^{N} \sum_{m=0}^{M} a_{nm} T_n(x) T_m(y), \tag{18}$$

$$\theta(t,x,y) = e^{\lambda t} \sum_{n=0}^{N} \sum_{m=0}^{M} b_{nm} T_n(x) T_m(y), \tag{19}$$

$$c(t,x,y) = e^{\lambda t} \sum_{n=0}^{N} \sum_{m=0}^{M} c_{nm} T_n(x) T_m(y), \tag{20}$$

where $T_k(x), k = 0,1,2\cdots$ are Chebyshev polynomials of the first kind. Depending on the dimensionless parameters, N and M vary in the range of 20–60 in order for the series to converge. By substituting Eqs. (18)–(20) into Eqs. (16) and (17), a generalized eigenvalue problem with a matrix size of $3(N+1)(M+1) \times 3(N+1)(M+1)$ is obtained. The complex eigenvalue λ can be determined when the parameters Re, Le, Pr and A are specified. Then one of the parameters, say Re, is

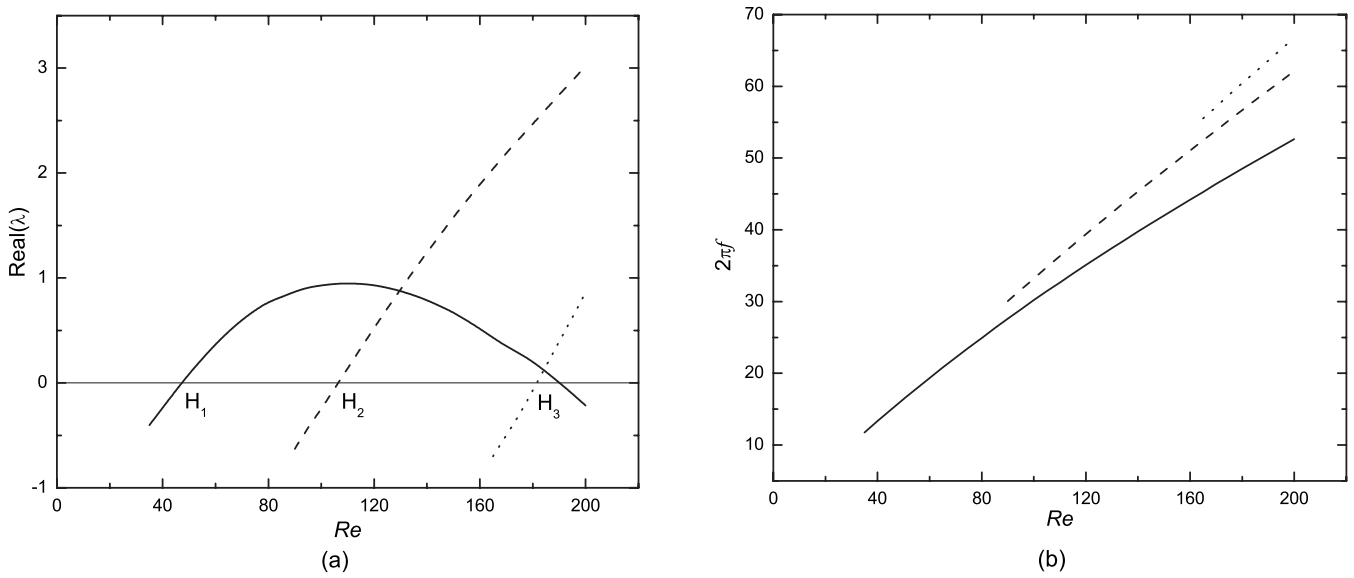

FIG. 2. Variation of (a) real parts and (b) imaginary parts of the most unstable eigenvalues with Re for Pr=5, Le=100 and $A=1/2$. H_1, H_2, and H_3 denote the onsets of the Mode I (thick solid line), Mode II (dashed line), and Mode III (dot line) oscillatory flows.

increased until the real part of λ vanishes. The corresponding value of Re is the critical condition for neutral stability and the imaginary part of λ, Im(λ), indicates whether the instability evolves into steady convection or growing oscillation. When the onset is oscillatory, the critical dimensionless oscillation frequency can be determined by $f_c=\mathrm{Im}(\lambda)/2\pi$.

Before applying this method to the complete problem, the Tau spectral method and the eigenvalue solving technique are used to solve the systems derived by Nield[24] and McTaggart[14] and validated by their known results. The results produced by the present methods are identical to those tabulated by Nield. The comparison with McTaggart's results is shown in Table I. It is noted that the factor Le was inadvertently left out of Eq. (2.1c) in McTaggart's paper, therefore the solutal Marangoni number B_S defined by her is related to our Ma_S by $\mathrm{Ma}_S=B_S/\mathrm{Le}$. Again the agreement is excellent.

IV. DIRECT NUMERICAL SIMULATION

Direct numerical simulation is also performed near the onset of instability to verify the linear stability results and to provide some additional information. Equations (2)–(6) together with the boundary conditions (7)–(11) are discretized using nonuniform control volumes. Finer grids cluster near the four boundaries in order to improve the numerical accuracy. Colocated variable arrangement is used and the SIMPLE algorithm is adopted to couple momentum and continuity equations. Details of the implementation of the numerical procedures can be found in Ferziger and Peric.[25]

In order to validate the code, the benchmark solution by Hortmann *et al.*[26] of natural convection of air in a square cavity is selected for comparison. These authors used very sophisticated numerical techniques including the full multigrid procedure, which allowed very fine grids (640×640) to be used, and finally the Richardson extrapolation was used to obtain grid-independent solutions. With 122×122 nonuniform grids, which have been verified to be able to produce grid-independent solution, all the present simulation results for Rayleigh number Ra equals to 10^4, 10^5, and 10^6 differ from the benchmark solutions by less than 0.05%.

V. RESULTS AND DISCUSSIOINS

A. Oscillatory flow regime

1. Variations of leading eigenvalues with Re

As the dynamic parameter Re increases, the eigenvalues in the complex plane move and it is the crossing of the rightmost eigenvalues with the imaginary axis that determines the onset of convection. Steady or oscillatory modes may be induced, depending on whether the crossing eigenvalues are real or complex. Thus it is interesting to see how the leading eigenvalues vary with Re. Following Bergman[20] we first consider the case Pr=5, Le=100, and $A=1/2$. For the range of Re considered in the present study, all the primary bifurcations are Hopf ones and we observe no steady onset of convection. The variations of the real and imaginary parts of the most unstable eigenvalues with Re are shown in Fig. 2. The equilibrium solution loses stability to the first oscillatory mode (Mode I) at H_1 ($\mathrm{Re}_c=48$) with a character-

TABLE I. Comparison of the present results with those of McTaggart (Ref. 14).

	$\mathrm{Ma}_s=-5$	$\mathrm{Ma}_s=0$	$\mathrm{Ma}_s=10$
McTaggart			
α	1.99	1.99	1.99
Ma	129.6	79.6	−20.4
Chebyshev-Tau			
α	1.99	1.99	1.99
Ma	129.607	79.607	−20.393

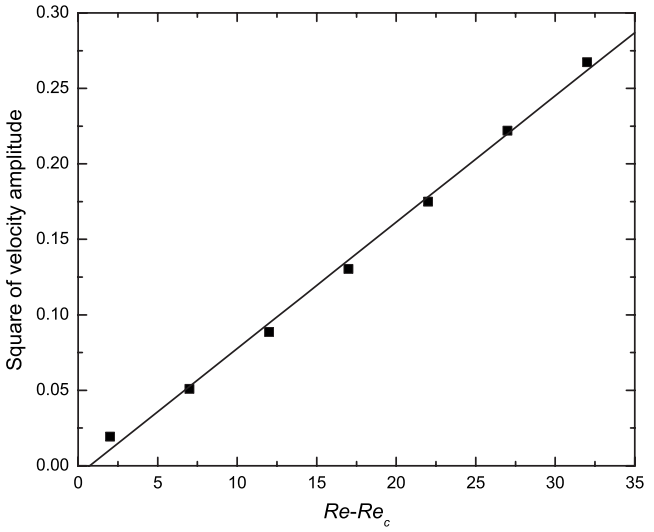

FIG. 3. Square of the amplitude of $u(t,0.5,0.5)$ vs $(\mathrm{Re}-\mathrm{Re}_c)$, where $\mathrm{Re}_c=48$ as predicted by linear stability analysis. Square points are obtained by direct numerical simulations while the solid line is the linear fit.

istic frequency $f_c=2.51$. It is interesting that the growth rate of this mode first increases and then decreases. With the increase in Re, the second (Mode II) and third (Mode III) oscillatory modes appear successively. It is only near the threshold H_1 that Mode I dominates the other modes. The corresponding frequencies of the three modes increase almost linearly with Re, as shown in Fig. 2(b).

It is well known that near a supercritical Hopf bifurcation, the amplitude of the periodic solution is $O(|\mathrm{Re}-\mathrm{Re}_c|^{1/2})$,[27] where Re_c is the critical Reynolds number at which a Hopf bifurcation occurs. Using the equilibrium solution as the initial fields, we start direct numerical simulations at Re=80, where the Mode I oscillation is dominant [Fig. 2(a)]. Then successive runs are performed for decreasing Re with a step of $\Delta\mathrm{Re}=5$, with the result of the last run as the initial fields of the next run. The square of the saturation amplitude of $u(t,0.5,0.5)$ versus the threshold departure $(\mathrm{Re}-\mathrm{Re}_c)$ is plotted in Fig. 3. The linear fit passes very close by the origin, which means that the direct simulation result agrees very well with the linear stability result and indeed the first critical point is a supercritical Hopf bifurcation.

In order to see clearly the flow structure of the Mode I oscillation, the flow fields at the end of eight successive equal time intervals totaling a full oscillation period at Re=50 are extracted and plotted in Fig. 4. Clockwise (dashed) and counterclockwise (solid) rotating vortices are periodically generated, traveling from right to left, and then squeezed into the upper left corner. As many as three vortices exist simultaneously in the flow field. In order to get the flow structure of the Mode II oscillation for comparison, direct simulation is performed at Re=150, where Mode II dominates Mode I [Fig. 2(a)]. The flow field shown in Fig. 5 again consists of clockwise and counterclockwise rotating vortices traveling from right to left, but with as many as five vortices exist simultaneously. The oscillation frequency is 7.81, which agrees quite well with the linear stability analysis result 7.69. At the same Re value, Mode II oscillates at a

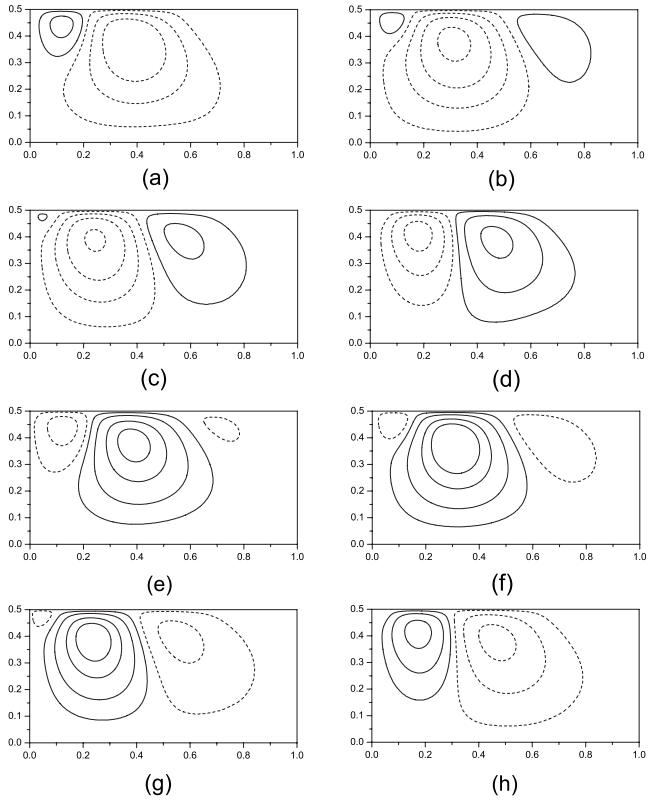

FIG. 4. Snapshots of the flow field at the end of eight successive equal time intervals totaling a full oscillation period at Re=50. Dashed and solid lines designate clockwise and counterclockwise rotations, respectively.

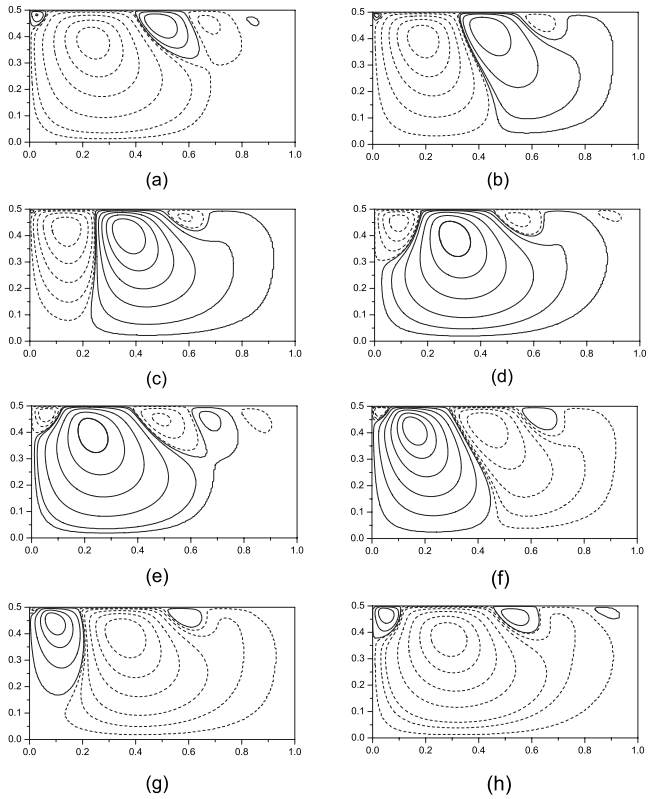

FIG. 5. The same as Fig. 4 but for Re=150.

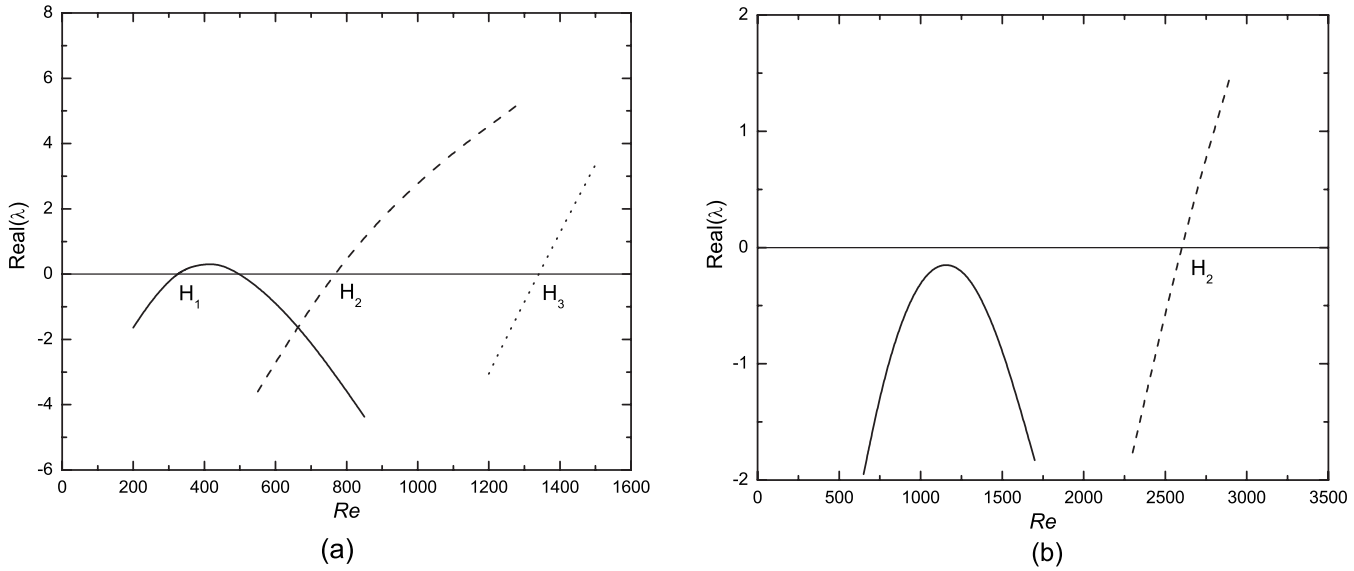

FIG. 6. The same as Fig. 2(a) but for (a) Le=5 and (b) Le=2.

higher frequency than Mode I does, as is clear from Fig. 2(b). One more different feature of Mode II is that the dominant vortex in the flow field can be so strong that it occupies almost the whole cavity, confining other counter-rotating vortices to the near-surface region [Figs. 5(d) and 5(h)]. This situation never occurs during the Mode I oscillation.

The variations of the real parts of the leading eigenvalues with Re when Le is changed to 5 and 2 are shown in Figs. 6(a) and 6(b), respectively. When Le=5 Mode I oscillation dies out quickly after its onset at H_1. Then the equilibrium solution regains its stability and the fluid becomes quiescent again until at H_2 where Mode II oscillation starts to grow. This strange behavior of returning to the pure conduction state as Re increases is quite unexpected and will be further discussed later. When Le=2 the growth rate of Mode I oscillation decreases before it becomes positive. Thus Mode I does not induce onset of convection and the equilibrium solution remains stable until H_2. In this case the flow that first appears is the Mode II oscillation. This situation is quite different from those when Le=100 and Le=5. In the next section we will investigate systematically the influences of A, Le, and Pr on the onsets of Mode I and Mode II.

2. Influences of A, Le, and Pr,

The influence of A on the onset of Mode I and Mode II when Pr=5 and Le=100 is shown in Fig. 7(a). The two curves qualitatively have the same shape. When A decreases from 0.5 the critical Re increases dramatically. When A is larger than 1 the two modes approach different asymptotic

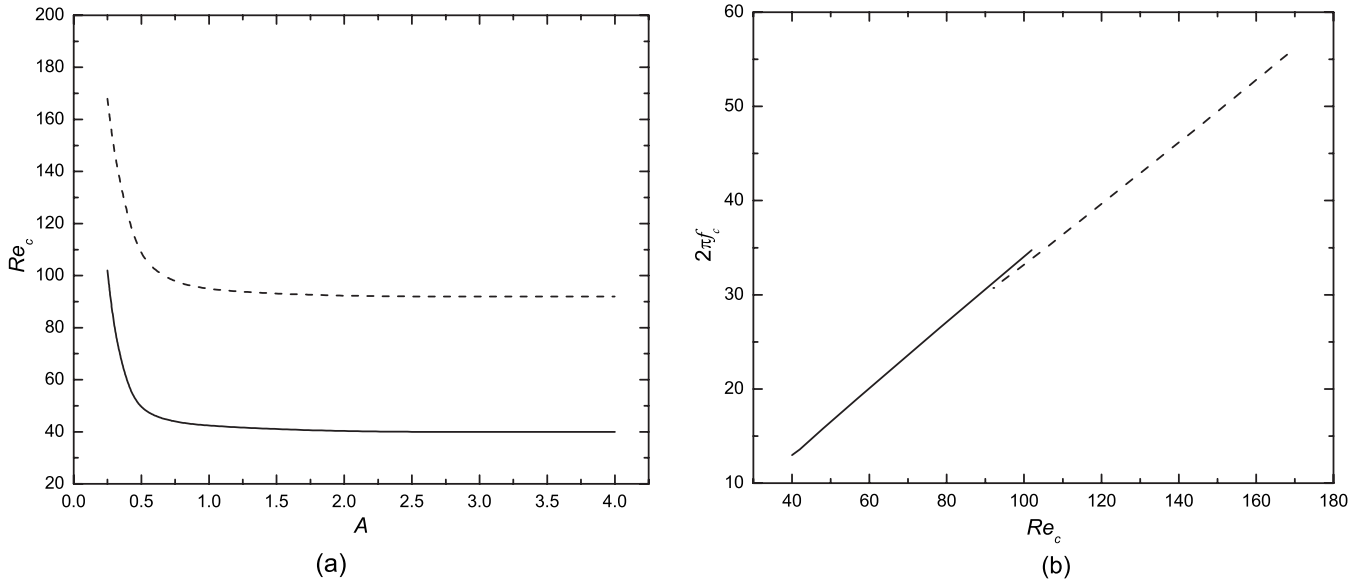

FIG. 7. Pr=5 and Le=100: (a) onset of Mode I (solid line) and Mode II (dashed line) with the variation of A and (b) the corresponding characteristic frequencies of the two modes vs the critical Re values.

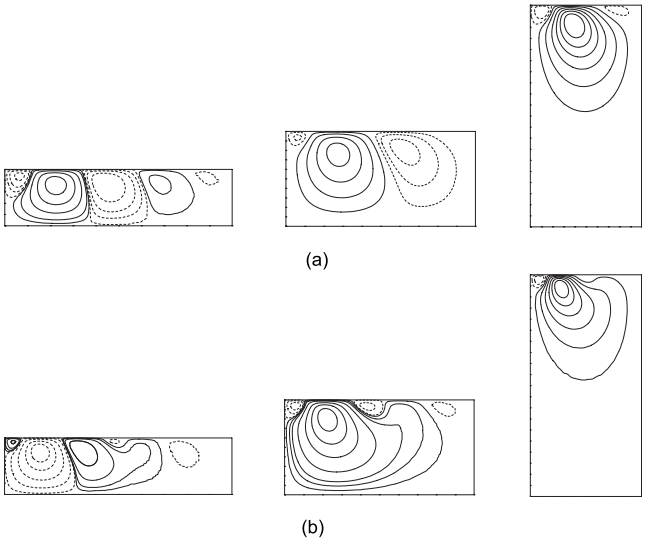

FIG. 8. Flow structures of the eigenfunctions for $A=1/4$, $A=1/2$, and $A=2$ when Pr=5 and Le=100: (a) Mode I and (b) Mode II.

states. The flow structures of the eigenfunctions for $A=1/4$, $A=1/2$, and $A=2$ are shown in Fig. 8. It is clear that for $A=1/2$, the flow fields of Mode I and Mode II at the onset are similar to Figs. 4(f) and 5(d), respectively, which are obtained by direct simulations. When $A=1/4$ more vortices simultaneously exist in the flow field. Because for even smaller A the assumed condition of a nondeformable liquid surface is questionable, $A=1/4$ is the smallest aspect ratio we have investigated. When $A=2$ flow only occurs in the upper half of the cavity while in the lower half the fluid is almost stagnant for both modes. For large aspect ratios the near surface flow structure decouples from what goes close to the bottom wall. This is why the flows approach asymptotic states when $A>1$ as shown in Fig. 7(a). The corresponding characteristic frequencies of the two different modes are shown in Fig. 7(b) as functions of Re_c. It is clear that f_c varies linearly with Re_c.Thus at smaller A where Re_c is higher, the flow oscillates with a higher frequency.

Usually with the increase in A in a confined cavity, neutral curves of the first two primary bifurcations will cross each other successively at codimension-two bifurcation points.[8,10,28–30] Thus the convective mode at the onset depends on the aspect ratio. However in our present case, the two curves in Fig. 7(a) are so well separated that they never cross each other in the range of parameters studied. The convective mode at the onset is always Mode I oscillation as shown in Fig. 8(a).

The influence of Le on the onset of Mode I and Mode II oscillations when Pr=5 and $A=1/2$ is shown in Fig. 9(a). The critical Re values for both modes decrease as Le increases, which means that at higher Le the modes are more unstable. This is reasonable and characteristic of double-diffusive instability because it is the difference of the diffusivity rates of the two components in the fluid that triggers the instability and Le denotes how large this difference is. When the difference vanishes (Le=1), the equilibrium is infinitely stable, as is apparent from Fig. 9(a) when Le decreases toward 1. The flow structures of the eigenfunctions of both modes for Le=5 and Le=100 are shown as insets. It is clear that the flow structures do not change qualitatively along the neutral curves. The corresponding characteristic frequencies of the two modes are shown in Fig. 9(b) as functions of Re_c. Unlike the situation in Fig. 7(b), f_c varies quadratically with Re_c in this case.

The influence of Pr on the onset of Mode I and Mode II oscillations when Le=100 and $A=1/2$ is shown in Fig. 10(a). This is plotted on a log-log scale since we are exploring low Pr number effect down to Pr=0.01. Because the ratio of the diffusivities of heat and solute has been fixed at 100, smaller Pr value means that heat and solute diffuse faster. Then infinitesimal disturbances of the temperature and con-

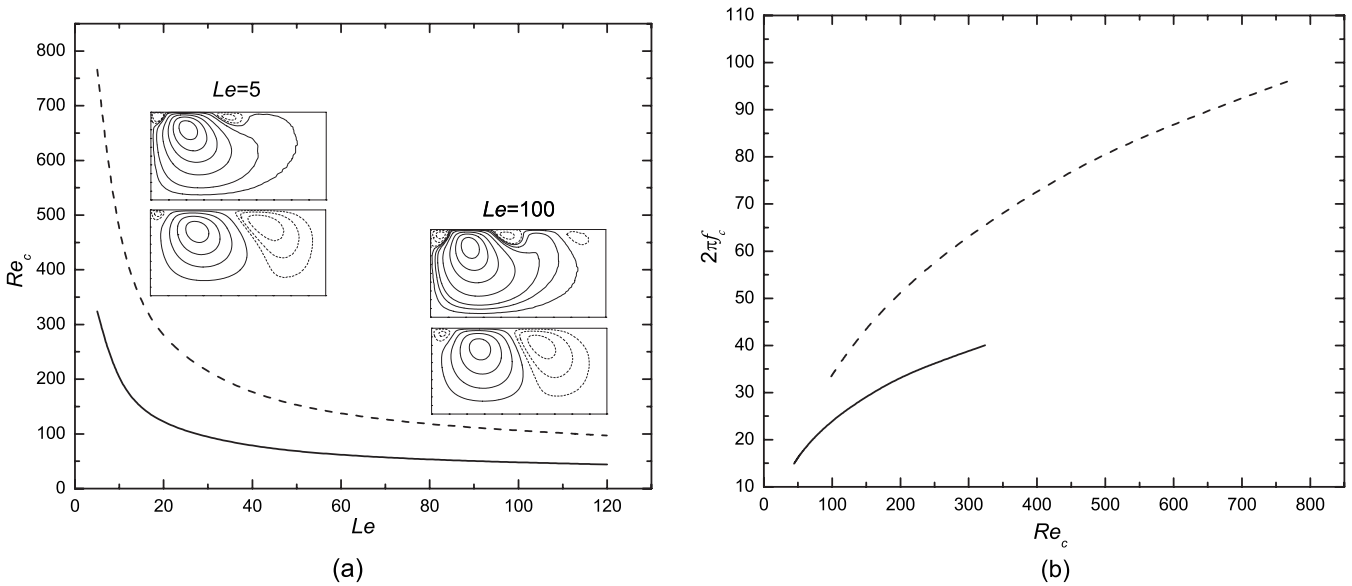

FIG. 9. Pr=5 and $A=1/2$: (a) onset of Mode I (solid line) and Mode II (dashed line) with the variation of Le (insets are the flow structures of the eigenfunctions at Le=5 and Le=100; lower ones are Mode I and upper ones are Mode II) and (b) the corresponding characteristic frequencies of the two different modes vs the critical Re values.

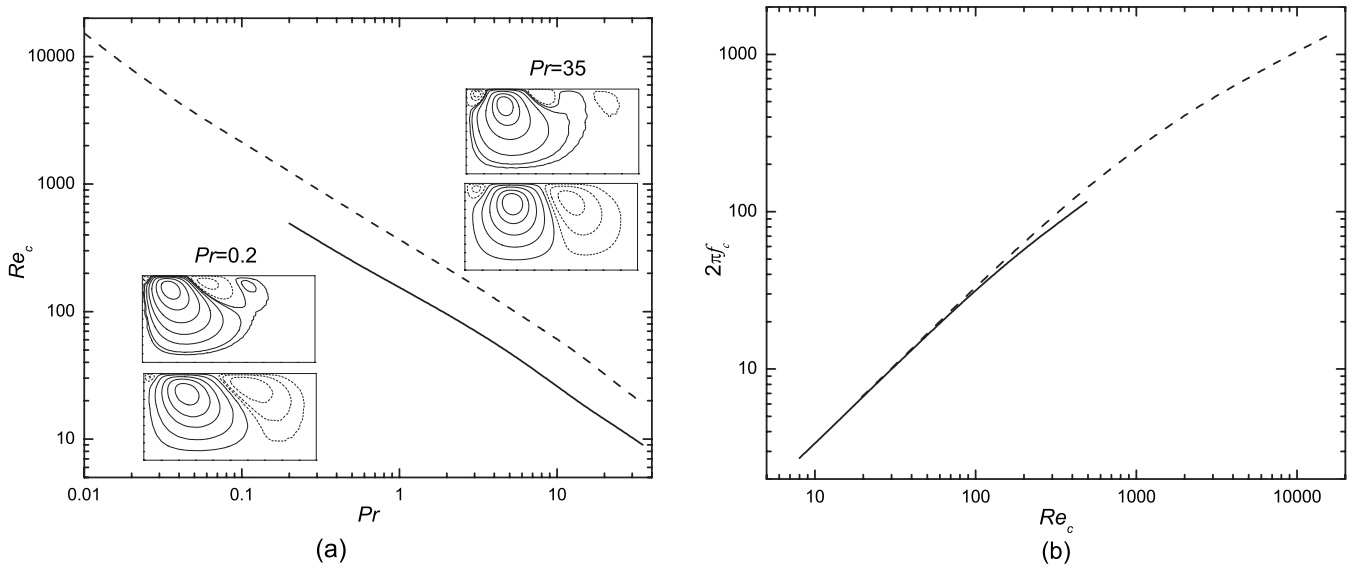

FIG. 10. Le=100 and $A=1/2$: (a) onset of Mode I (solid line) and Mode II (dashed line) with the variation of Pr (insets are the flow structures of the eigenfunctions at Pr=0.2 and Pr=35; lower ones are Mode I and upper ones are Mode II) and (b) the corresponding characteristic frequencies of the two oscillatory modes vs the critical Re values.

centration field can be dissipated faster, rendering the equilibrium solution more stable. The most distinctive difference between Figs. 10(a) and 7(a) or Fig. 9(a) is that Mode I oscillation disappears for low Pr values. This mode disappearance is the situation described in Fig. 6(b). Because the growth rate of Mode I remains negative, Mode II oscillation is responsible for the first onset of convection. For the present parameter combination of Le=100 and $A=1/2$, Mode I oscillation exists down to roughly Pr=0.2 and the solid curve in Fig. 10(a) terminates at this point. The insets show the flow structures of the eigenfunctions for both modes at Pr=0.2 and Pr=35. As in Fig. 9(a), the flow structures do not change qualitatively along the two neutral curves, except that the vortices at low Pr number are more inclined toward the left vertical wall. The corresponding characteristic frequencies of the two modes are shown in Fig. 10(b). They vary almost linearly with Re_c in this log-log scale.

Now it is clear that it is not always Mode I that is responsible for the first onset of convection. Mode II is sometimes responsible for the first onset. This is not because the neutral curves representing the onset of these two modes cross each other at codimension-two points, but that the growth rate of Mode I does not get positive. The missing of Mode I at low Pr values in Fig. 10(a) necessitates the need to derive a more complete picture showing the mode type of the first onset of convection in a more complete parameter space. By selecting $A=1/2$ as the representative case, Fig. 11 shows the Le-Pr plane separated by a curve, above and below which the first onset of convection is Mode I and Mode II, respectively. It is clear that for a fixed Pr value, the Le value needs to be large enough for Mode I to onset. This is also the situation we have seen in Figs. 2(a) and 6. More important is that from Fig. 11 we can easily assess the mode type at the first onset of convection when the fluid properties are known. For example in a heat and mass transfer system, the Le value is typically 100. Then if the fluid is a water-based solution whose Pr value is O(10), the first onset of convection is Mode I; if the fluid is a semiconductor crystal melt whose Pr value is O(0.01), the first onset of convection is Mode II. This piece of information has very useful engineering applications.

3. Instability mechanism

It has been seen in Figs. 4 and 5 that for the two different oscillatory modes, counter-rotating vortices are generated alternately near the liquid surface. These vortices grow in size first and then decay as they move toward the left vertical wall. Finally they are all squeezed into the upper-left corner of the cavity and disappear. The physical mechanism of the onset of instability is described below.

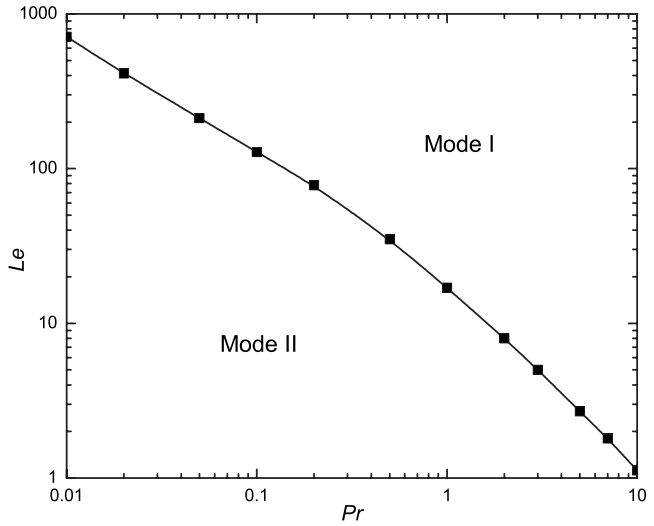

FIG. 11. Determination of the different modes of the first onset of convection in the Le-Pr plane for $A=1/2$.

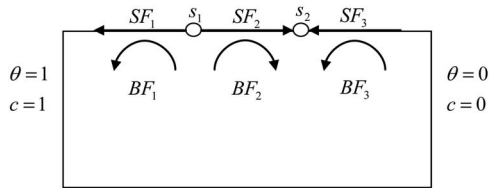

FIG. 12. Physical illustration of the instability mechanism. SF_1, SF_2, and SF_3 denote surface flows; BF_1, BF_2, and BF_3 denote bulk flows; s_1 and s_2 denote the relatively fresh and dense spots, respectively.

In the present study, Re is positive while Re_S is negative, which means that liquid surface tension decreases with temperature and increases with solute concentration. For the boundary conditions specified, the temperature gradient tends to drag the surface liquid from left to right while the concentration gradient tends to act in the opposite direction. $R_\sigma=-1$ means that these two effects exactly balance each other, resulting in the equilibrium solution. Since small disturbance is always present and heat has a greater diffusivity over that of solute, it is easier for the uniform solute concentration gradient to be disturbed. Suppose a fresher spot s_1 appears on the liquid surface, as shown in Fig. 12, then *locally* the concentration gradient on its left-hand side is increased and that on its right-hand side is decreased. Surface flows, SF_1 and SF_2, leaving s_1 in opposite directions are thus generated, inducing the corresponding bulk flow BF_1 and BF_2 by viscosity. SF_1 points in the direction of the base concentration gradient, bringing relatively fresh fluid into contact with denser fluid, and thus the enhanced concentration gradient region moves leftwards. This surface flow can reach the left vertical wall. SF_2, however, points in the opposite direction of the base concentration gradient and thus brings relatively denser fluid into contact with fresher fluid. The dense fluid front s_2 will in turn induce another surface flow SF_3 and bulk flow BF_3, since the concentration gradient on the right hand side of s_2 is locally enhanced. Thus SF_2 cannot reach the right vertical wall because of the opposing flow SF_3. Similarly, if a denser spot s_2 first appears on the liquid surface, the same surface and bulk flows will be generated. Additionally, s_1 and s_2 cannot remain stationary. They are in locally enhanced concentration gradients because of the bulk flows, BF_1 and BF_2, and surface flows, SF_2 and SF_3. Thus s_1 and s_2, together with the counter-rotating vortices, move toward the left vertical wall. This whole scenario matches the development of the flow fields shown in Figs. 4 and 5. The gradient of the solute concentration together with the sign of Re_S determine the traveling direction.

The above physical illustration clearly explains the instability mechanism of the onset of oscillatory flows. We might expect an even more destabilizing mechanism when Re increases and thus the reverse transition from Mode I oscillatory flow to quiescent equilibrium at Re=512 in Fig. 6(a) appears to be counterintuitive. Although the linear stability analysis procedure was carefully verified before being used and it produces results that agree very well with direct numerical simulations, as discussed in the preceding sections, we are particularly careful about this puzzling reverse transition and further direct numerical simulations were performed to verify the scenario presented in Fig. 6(a), where Re is 325 and 766 at H_1 and H_2, respectively. As shown in Fig. 13, direct numerical simulation is started from the equilibrium solution with Re=300. The fluid remains motionless and at $t=10$ Re is increased to 350. Then oscillation starts to grow and saturates at about $t=40$. At $t=50$ Re is increased to 410 and the flow starts to oscillate with a larger amplitude. As predicted in Fig. 6(a), when Re is increased to 500 at $t=60$ the oscillation amplitude decreases, and when Re is further increased at $t=75$ to 540, which is larger than the reverse transition threshold 512, the oscillation exponentially decays and finally the equilibrium solution is regained. The flow fields of the oscillations in the interval $20<t<80$ for different Re values were carefully investigated and they all correspond to Mode I oscillation, as shown in Fig. 4. The fluid remains motionless after Re is increased to 730 at $t=90$. Finally, when Re is further increased to 780 at $t=100$ Mode II oscillation starts to grow. This whole transition scenario is exactly as that predicted in Fig. 6(a). Also, the oscillation frequencies in Fig. 13 for different Re values all agree very well with those predicted by linear stability analysis (Table II). The transition scenario in Fig. 2(a) will be later further verified in Fig. 16 by showing the maximum stream function value.

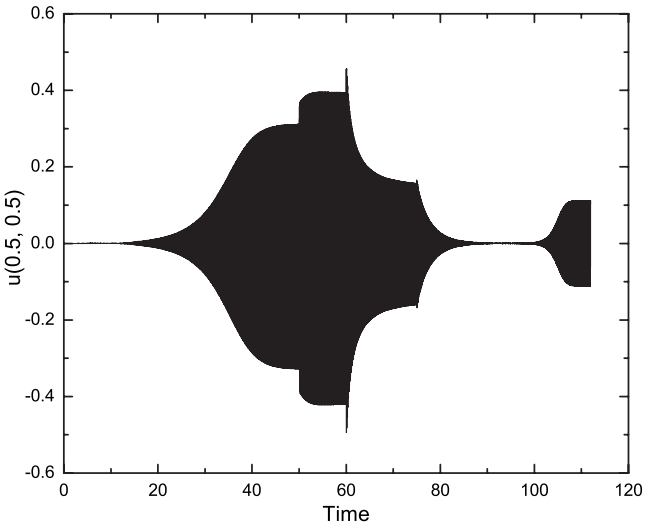

FIG. 13. Direct numerical simulation starting from the equilibrium solution with Re=300 for Pr=5, Le=5 and $A=1/2$. Then Re is changed to 350 at $t=10$, to 410 at $t=50$, to 500 at $t=60$, to 540 at $t=75$, to 740 at $t=90$, and finally to 780 at $t=100$. For the long evolution time shown, the oscillations are so closely packed that only the envelope can be discerned.

For Rayleigh–Bénard convection in small aspect ratio enclosure, reverse transition from two-frequency quasiperiodic flow to steady flow with the increase in Rayleigh number (Ra) was observed experimentally by Gollub and Benson.[31] This counterintuitive transition was later reproduced numerically by Mukutmoni and Yang,[32] where it was found that the transition was accompanied by a change of the flow field to a more complex spatial form. Then it was argued that the overall complexity of the system increases, even though the temporal complexity reduces, and so there was no paradox or anomaly. In our present study, the spatial form of Mode II oscillation (Fig. 5) is obviously more com-

TABLE II. Comparison of the oscillation frequencies obtained by direct numerical simulation (DNS, Fig. 13) and linear stability analysis (LSA).

	Re				
	350	410	500	540	780
DNS	6.84	7.82	9.26	10.02	15.58
LSA	6.80	7.78	9.21	9.98	15.53

plex than that of Mode I (Fig. 4), five vortices versus three vortices. As shown in Figs. 2(a) and 6, even though the growth rate of Mode I first increases and then decreases, the growth rates of Mode II and Mode III keep increasing. Thus it *might* be argued that the overall complexity of the system increases.

One more argument that *might* be helpful for understanding the reverse transition is as follows. In the present double-diffusive Marangoni problem, R_σ is always equal to -1. This is very different from the case when $R_\sigma \neq -1$, say when $R_\sigma = -0.5$ and the overall forcing of the system is $\mathrm{Re} + \mathrm{Re}_S = 0.5\mathrm{Re}$, or from the Rayleigh–Bénard problem, where Ra is the only external forcing parameter. In these two cases when Re or Ra increases, the overall external forcing of the respective system increases and the system should become more and more complex. In our present problem, however, when Re increases, the overall forcing of the system always remains zero. Thus there is no guarantee that the overall complexity of the system should keep increasing *monotonically*.

Figure 12 illustrates qualitatively the formation and propagation of counter-rotating vortices. It is difficult to use such qualitative illustration to differentiate the onset of Mode I and Mode II oscillations, which depends quantitatively on the physical properties of the fluid (Fig. 11). Especially it is difficult to assess the influence of the lateral walls and determine the number of vortices confined in the cavity. Also, the damping of Mode I might involve the interaction with even higher order modes, like Mode III and so on, which are not investigated in the present work. Thus the physical mechanism for the damping of Mode I is not clear in the present study.

Linear stability analysis and direct simulation, together with the physical illustration in Fig. 12, clearly show that the onset of instability is oscillatory. However, Bergman[20] studied the case Pr=5, Le=100, and $A=1/2$ by direct simulation and obtained steady flow with Ma=1000, which corresponds to $\mathrm{Re}=\mathrm{Ma}/\mathrm{Pr}=200$ and is larger than the critical value $\mathrm{Re}_c = 48$ by linear stability analysis. This is quite contradictive and in the next section we will discuss in detail how the onset of steady flow arises.

B. Steady flow regime

So far the direct numerical simulations have been performed with the equilibrium solution as the initial field. The resultant flows are oscillatory, which agree well with the linear stability analysis. When direct simulation starts from the all-zero initial field $u=v=p=\theta=c=0$, a totally different flow regime is obtained. This is shown in Fig. 14 using these two different initial fields while keeping all the control parameters the same. The oscillatory flow in Fig. 14(a) oscillates in Mode II since this is the fastest growing mode at Re=200, as is clear from Fig. 2(a). The corresponding flow field is qualitatively the same as that in Fig. 5. In Fig. 14(b), after the initial transition stage, the flow finally approaches steady state. The steady state flow fields are presented in Fig. 15. This is the steady solution obtained by Bergman[20] (refer to

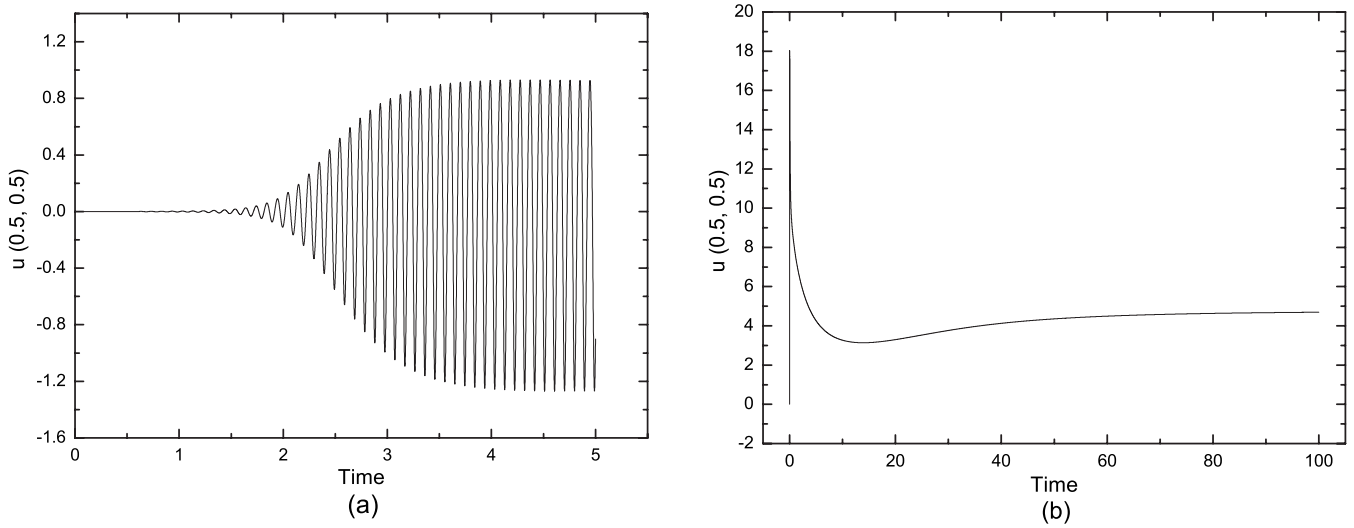

FIG. 14. Time series of $u(t,0.5,0.5)$ for Re=200, Le=100, Pr=5, and $A=1/2$, with (a) the equilibrium solution (b) $u=v=p=\theta=c=0$ as the initial field.

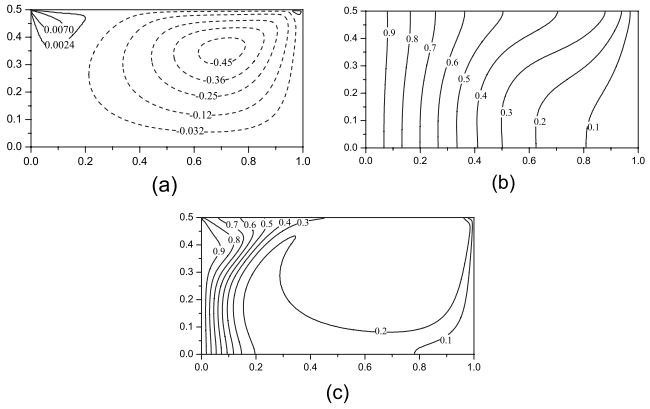

FIG. 15. Contours of (a) stream function, (b) temperature, and (c) solute concentration for Re=200, Le=100, Pr=5, and $A=1/2$ (steady flow regime).

his Fig. 2). Since the simulation starts from the all-zero initial field and heat diffuses 100 times faster than solute does, the temperature gradient is quickly established across the surface and the clockwise rotating vortex is generated. This happens in an extremely short time, which can be seen from the position of the peak in Fig. 14(b). As solute slowly diffuses, a small counterclockwise rotating vortex in the upper left corner of the cavity develops. However finally it cannot compete with the fully established clockwise rotating vortex and is thus confined to the upper-left corner.

Using the maximum stream function as the measure, the simultaneous existence of the two different flow regimes, oscillatory and steady flows, is shown in Fig. 16 for Le =100, Pr=5, and $A=1/2$. The direct simulation of the oscillatory flow continues from the results shown in Fig. 3, using the result obtained as the initial field of the next run for increasing Re. The magnitude of ψ_{max} increases first and then decreases, as predicted in Fig. 2(a). At Re=150 the flow starts to oscillate in Mode II, since this is the fastest growing mode at this Re value [Fig. 2(a)]. The steady flows are calculated starting from Re=200 (Fig. 15) with decreasing and increasing Re. Time stepping is switched off for fast convergence. This steady flow branch terminates at Re=55, below which convergence fails. With the all-zero initial field, the time stepping at a slightly smaller value Re=52 confirms that the flow finally reaches the pure conductive equilibrium solution (Fig. 17).

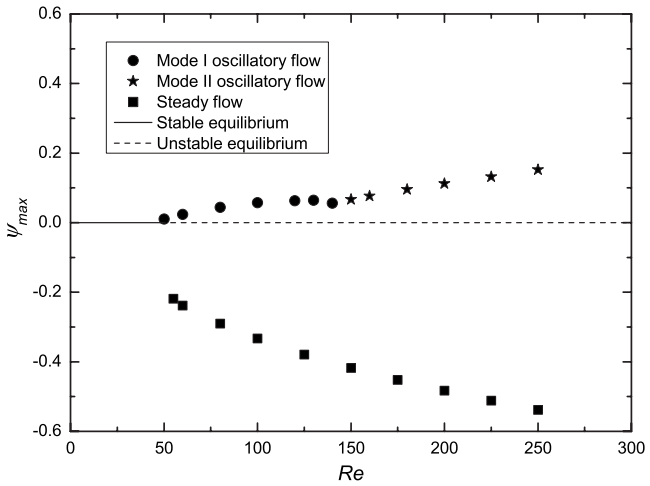

FIG. 16. Maximum stream function vs Re, showing the simultaneous existence of the steady and oscillatory flow regimes (Le=100, Pr=5, $A=1/2$).

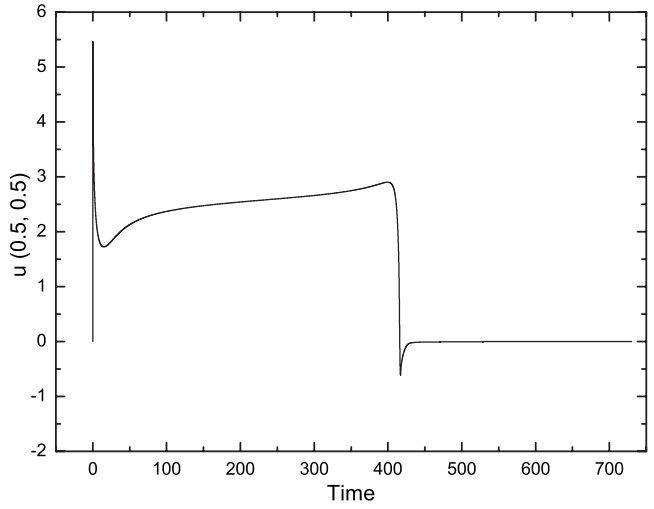

FIG. 17. Time series of $u(0.5,0.5)$ for Re=52, Le=100, Pr=5, and $A=1/2$ with $u=v=p=\theta=c=0$ as the initial field.

As is seen from Fig. 16, the oscillatory flow bifurcating from the equilibrium solution arises from small disturbances while the steady flow is induced by finite amplitude disturbance. The steady flow is much more vigorous than the oscillatory one at the same Re value. In the present study, the origin of the steady flow branch and its relation with the oscillatory flow branches are unclear. For the eigenvalue problem, usually the complex pair of eigenvalues splits into two real eigenvalues for larger Re. One of the emerging real eigenvalues keeps increasing with Re while the other one decreases, producing a steady subcritical bifurcation responsible for the existence of subcritical steady flow branches.[30,33] Unfortunately this scenario does not hold here, at least in the range of Re values investigated [Fig. 2(a)].

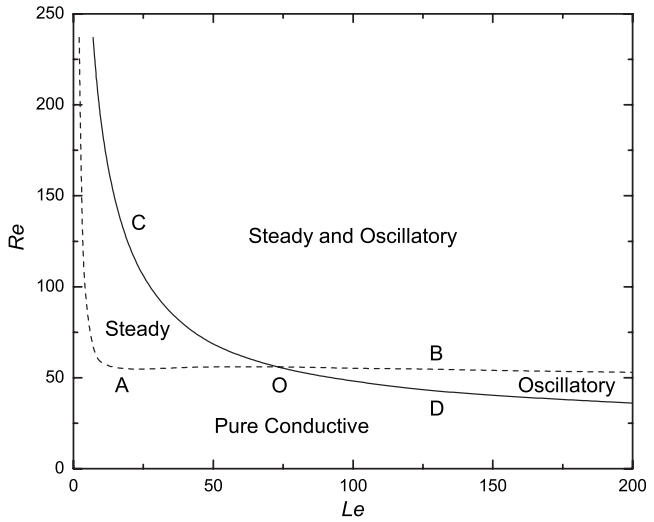

FIG. 18. Onset of steady (dashed line) and Mode I oscillatory (solid line) flows as Le increases for Pr=5 and $A=1/2$.

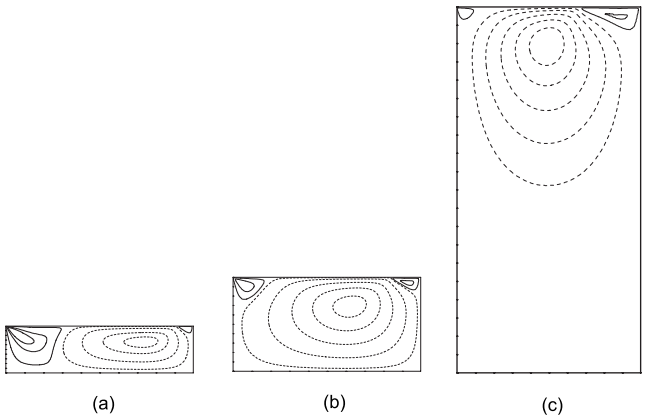

FIG. 19. Steady flow fields near the onset of steady state convection for Pr=5 and Le=100: (a) $A=1/4$ (Re=135), (b) $A=1/2$ (Re=55), and (c) $A=2$ (Re=77).

Otherwise the coexistence of steady and oscillatory states is an obvious consequence. We are currently developing a continuation method to generate a more complete bifurcation diagram to fully explore the different solution branches.

The onset of the steady flow with the variation of Le is shown in Fig. 18, together with the neutral curve in Fig. 9(a) for the onset of the Mode I oscillatory flow. These two curves separate the Re-Le plane into four parts: below AOD, the equilibrium is stable and the fluid is in a pure conductive state; above AO and below CO when starting from the all-zero initial field, steady flows are obtained; above OD and below OB when starting from the equilibrium solution, oscillatory flows are obtained; and above COB, both steady and oscillatory flows are possible, depending on the initial field. The critical point O is located at Le=73. For $\mathrm{Le}<73$ the first onset of convection is steady flow while for $\mathrm{Le}>73$ the first onset of convection is oscillatory flow.

Finally the steady flow fields near the onset of steady state convection for different cavity aspect ratios are shown in Fig. 19. While the thermal Marangoni effect is dominant over most part of the upper surface, creating the large clockwise rotating vortices, the solutal Marangoni effect is only dominant near the vertical walls, generating the much smaller counterclockwise rotating vortices. As in the oscillatory flow regime (Fig. 8), the steady flow field approaches an asymptotic state as A becomes large, since the near-surface flow structure separates from what goes close to the cavity bottom [Fig. 19(c)]. For aspect ratios in the range $1/4<A<4$ studied in the present work, we only observed one steady solution type (Fig. 19). This is very different from the counterpart buoyant convection problem,[6] in which many stable subcritical steady state solutions exist for the same aspect ratio: a phenomenon known as homoclinic snaking.[34,35]

VI. CONCLUSIONS

In the present paper the onset of double-diffusive Marangoni convection in a rectangular cavity with horizontal temperature and concentration gradients is studied. The opposing case $R_\sigma=-1$ in which the equilibrium solution can remain stable up to a critical thermal surface tension Reynolds number Re_c is considered. Direct numerical simulations using the full nonlinear governing equations as well as linear stability analysis are used to study the problem. The main results of the present study are summarized as follows:

(1) Variations of the leading eigenvalues with Re for different Le values are shown. The increase in Re can first destabilize and then stabilize the Mode I oscillatory flow, the growth rate of which can sometimes never get positive. The first three most unstable modes are all oscillatory.
(2) Neutral stability curves for the onset of the first two oscillatory modes, showing the influences of A, Le, and Pr, are obtained, together with the flow fields of the bifurcating eigenfunctions. The first onset of convection can be Mode II oscillatory flow, not because that the neutral stability curves of the two modes cross each other, but that the Mode I oscillatory flow does not get onset.
(3) A simple physical illustration is provided to demonstrate the instability mechanism when $\mathrm{Re}>\mathrm{Re}_c$. The formation of counter-rotating vortices traveling from right to left in the present configuration is explained.
(4) Steady and oscillatory flow regimes simultaneously exist in the Re range studied. The oscillatory flow resulting from a supercritical Hopf bifurcation point is generated by small disturbance, while the steady flow is induced by finite amplitude disturbance. Only one type of steady state solution is observed in the present study.

Bergman's original work[20] left many unsolved issues and the present work tries to resolve some of them. The present double-diffusive Marangoni problem can be considered a prototype configuration relevant to materials processing, e.g., crystal growth in a low-gravity environment. When growing crystals from melts and aqueous solutions, convective flow is in general beneficial, since it serves to reduce the diffusional barrier; while it has been found experimentally that when the flow is oscillatory there are marked impurity striations in the resultant crystals.[14] The present study shows that the initial field can be used to control the nature of the flow, steady or oscillatory, while other conditions remain the same.

ACKNOWLEDGMENTS

The work reported in this paper is supported by the National Science Foundation of China (Grant No. 40476012) and the Research Grants Council of the Hong Kong Special Administrative Region, China (Project No. PolyU 5220/07E).

[1] J. S. Turner, "Double-diffusive phenomena," Annu. Rev. Fluid Mech. **6**, 37 (1974).
[2] H. E. Huppert and J. S. Turner, "Double-diffusive convection," J. Fluid Mech. **106**, 299 (1981).
[3] J. S. Turner, "Multicomponent convection," Annu. Rev. Fluid Mech. **17**, 11 (1985).
[4] R. Krishnan, "A numerical study of the instability of double diffusive convection in a square enclosure with a horizontal temperature and concentration gradients," *ASME National Heat Transfer Conference*, Philadelphia, 1989 (ASME, New York, 1989), p. 357.

[5]D. Gobin and R. Bennacer, "Double diffusion in a vertical fluid layer: Onset of the convective regime," Phys. Fluids **6**, 59 (1994).
[6]K. Ghorayeb and A. Mojtabi, "Double diffusive convection in a vertical rectangular cavity," Phys. Fluids **9**, 2339 (1997).
[7]K. Ghorayeb, H. Khallouf, and A. Mojtabi, "Onset of oscillatory flows in double-diffusive convection," Int. J. Heat Mass Transfer **42**, 629 (1999).
[8]S. H. Xin, P. Le Quere, and L. S. Tuckerman, "Bifurcation analysis of double-diffusive convection with opposing horizontal thermal and solutal gradients," Phys. Fluids **10**, 850 (1998).
[9]G. Bardan, A. Bergeon, E. Knobloch, and A. Mojtabi, "Nonlinear doubly diffusive convection in vertical enclosures," Physica D **138**, 91 (2000).
[10]A. Bergeon, K. Ghorayeb, and A. Mojtabi, "Double diffusive instability in an inclined cavity," Phys. Fluids **11**, 549 (1999).
[11]M. Karimi-Fard, M. C. Charrier-Mojtabi, and A. Mojtabi, "Onset of stationary and oscillatory convection in a tilted porous cavity saturated with a binary fluid: Linear stability analysis," Phys. Fluids **11**, 1346 (1999).
[12]S. H. Davis, "Thermocapillary instabilities," Annu. Rev. Fluid Mech. **19**, 403 (1987).
[13]J. R. A. Pearson, "On convection cells induced by surface tension," J. Fluid Mech. **4**, 489 (1958).
[14]C. L. McTaggart, "Convection driven by concentration- and temperature-dependent surface tension," J. Fluid Mech. **134**, 301 (1983).
[15]K.-L. Ho and H.-C. Chang, "On nonlinear double-diffusive Marangoni instability," AIChE J. **34**, 705 (1988).
[16]C. F. Chen and T. F. Su, "Effect of surface tension on the onset of convection in a double-diffusive layer," Phys. Fluids A **4**, 2360 (1992).
[17]J. Tanny, C. C. Chen, and C. F. Chen, "Effects of interaction between Marangoni and double-diffusive instabilities," J. Fluid Mech. **303**, 1 (1995).
[18]C. F. Chen and F. L. Chen, "Salt-finger convection generated by lateral heating of a solute gradient," J. Fluid Mech. **352**, 161 (1997).
[19]C. L. Chan and C. F. Chen, "Salt-finger convection generated by thermal and solutal capillary motion in a stratified fluid," Int. J. Heat Mass Transfer **42**, 2143 (1999).
[20]T. L. Bergman, "Numerical simulation of double-diffusive Marangoni convection," Phys. Fluids **29**, 2103 (1986).
[21]K. Arafune and A. Hirata, "Interactive solutal and thermal Marangoni convection in a rectangular open boat," Numer. Heat Transfer, Part A **34**, 421 (1998).
[22]K. Arafune, K. Yamamoto, and A. Hirata, "Interactive thermal and solutal Marangoni convection during compound semiconductor growth in a rectangular open boat," Int, J. Heat Mass Transfer **44**, 2405 (2001).
[23]C. Canuto, M. Y. Hussaini, A. Quarteroni, and T. A. Zang, *Spectral Methods in Fluid Dynamics* (Springer, New York, 1988).
[24]D. A. Nield, "Surface tension and buoyancy effects in cellular convection," J. Fluid Mech. **19**, 341 (1964).
[25]J. H. Ferziger and M. Peric, *Computational Methods for Fluid Dynamics* (Springer-Verlag, Berlin, 2002).
[26]M. Hortmann, M. Peric, and G. Scheuerer, "Finite volume multigrid prediction of laminar natural convection: Bench-mark solutions," Int. J. Numer. Methods Fluids **11**, 189 (1990).
[27]J. Guckenheimer and P. Holmes, *Nonlinear Oscillations, Dynamical Systems, and Bifurcations of Vector Fields* (Springer, New York, 1983).
[28]K. H. Winters, T. Plesser, and K. A. Cliffe, "The onset of convection in a finite container due to surface tension and buoyancy," Physica D **29**, 387 (1988).
[29]H. A. Dijkstra, "On the structure of cellular solutions in Rayleigh-Benard-Marangoni flows in small-aspect-ratio containers," J. Fluid Mech. **243**, 73 (1992).
[30]A. Bergeon, D. Henry, H. Benhadid, and L. S. Tuckerman, "Marangoni convection in binary mixtures with soret effect," J. Fluid Mech. **375**, 143 (1998).
[31]J. P. Gollub and S. V. Benson, "Many routes to turbulent convection," J. Fluid Mech. **100**, 449 (1980).
[32]D. Mukutmoni and K. T. Yang, "Thermal convection in small enclosures: An atypical bifurcation sequence," Int. J. Heat Mass Transfer **38**, 113 (1995).
[33]L. S. Tuckerman, "Thermosolutal and binary fluid convection as a 2×2 matrix problem," Physica D **156**, 325 (2001).
[34]O. Batiste and E. Knobloch, "Simulations of localized states of stationary convection in ^{3}He–^{4}He mixtures," Phys. Rev. Lett. **95**, 244501 (2005).
[35]A. Bergeon and E. Knobloch, "Spatially localized states in natural doubly diffusive convection," Phys. Fluids **20**, 034102 (2008).